Investigations on the corrosion of 316L steel composite materials with MgO/TiO$_2$ ceramic immersed in molten cryolite

C. Weigelt [a,*], S. Yaroshevskyi [a], F. Kerber [a], N. Brachhold [a], T. Zienert [a], A. Adamczyk [b], D. Vogt [b], A. Charitos [b], C.G. Aneziris [a]

[a] Institute of Ceramics, Refractories and Composite Materials, Technische Universität Bergakademie Freiberg, Germany
[b] Institute of Nonferrous Metallurgy and Purest Materials, Technische Universität Bergakademie Freiberg, Germany

ARTICLE INFO

ABSTRACT

Composites based on a steel with 40 vol% magnesia or titania were produced with the ceramics-derived extrusion and pressureless sintering. The materials were tested in a laboratory-scale fused-salt electrolysis cell with a synthetic cryolite in order to identify their potential use as electrode material in the Hall-Héroult process. The highly corrosive atmosphere and salt melt initiated certain corrosion effects in both material variants. The corrosion depth was determined with 1160 μm for magnesia and 463 μm for titania, respectively, after 8 h corrosion test. The initial corrosion includes the complete penetration of the specimens with cryolite and the dissolution of the ceramic component. A pre-oxidation of the specimens containing magnesia depressed the corrosion depth by 75% due to the formation of an aluminium oxide layer in the composite material during corrosion tests. The reduction in corrosion depth by pre-oxidation was less pronounced for the TiO$_2$ composite materials (−15%).

1. Introduction

Aluminium is present in everyday life due to advantageous properties such as the low density, high corrosion resistance, easy processing, high mechanical strength, heat and electrical conductivity, non-toxicity, and recyclability. A large range of products covering construction, electronics, packaging, automotive and transportation demands increasing amounts of pure aluminium. Aluminium is one of the most common elements in earth's crust, but naturally never appears in elementary form. Efficient processing of primary aluminium includes the leaching of aluminium ore (bauxite) with caustic soda and the subsequent filtration and crystallisation. The resulting pure alumina (Al$_2$O$_3$) is the starting material for fused-salt electrolysis (Hall-Héroult process) where the aluminium oxide is converted to metallic aluminium. The production unit consists of the electrolytic cell with the melting container and graphite bottom cathode, the blocky graphite anode, the exhaust gas fume hood, the cryolite-alumina mixture and the resulting molten aluminium [1].

Cryolite (Na$_3$AlF$_6$) is the industrial standard electrolyte for aluminium production. Mixtures of roughly 11 wt% Al$_2$O$_3$ and cryolite provide an eutectic melting at approx. 960 °C. The ratio of Na$_3$AlF$_6$/Al$_2$O$_3$ crucially affects the efficiency and the processing of the electrolysis cell. Small fractions of additional components, such as calcium fluoride (CaF$_2$), lithium fluoride (LiF), aluminium fluoride (AlF$_3$), are used to modify the technical features of the salt, e.g. the melting point, the density, the electrical conductivity, and of the Al$_2$O$_3$ solubility. The additives also tremendously change the economics of the aluminium production. The molar cryolite ratio (CR = n(NaF)/n(AlF$_3$)) of industrial bath is usually decreased from 3 in pure cryolite to CR = 2–3 with 5–15 wt% excess AlF$_3$ [1].

The aluminium smelting flux electrolysis is covered by extensive corrosion mechanisms induced by the highly corrosive melts and the inevitable vaporisation of some components (e.g. NaAlF$_4$) [1]. Common technologies use carbon for both, the anode and the cathode. Yet, the use of carbon anodes is closely related to several economic and environmental disadvantages in the energy-intensive aluminium production. The continuous consumption of carbon is associated with the intensive formation of carbon monoxide (CO) and carbon dioxide (CO$_2$). These emissions (ranging ≈5–20 tonnes CO$_2$/tonne Al) are strongly influenced by the source of the electrical power supply according to calculations of

Kvande and Haupin [2]. Thus, changing the source of power enables a certain reduction of CO_2 emissions. However, emissions from the electrolysis process of carbon anodes are unavoidable. Beyond, inappropriate conditions favour the formation of perfluorocarbon (PFC) greenhouse gases, such as CF_4 and C_2F_6 when using carbonaceous anodes.

Efforts to carry the established fused-salt electrolysis to carbon-free technology include the replacement of carbon anodes by carbon-free materials, so-called inert anodes. Investigations in recent years on the invention of inert anodes led to three main groups of materials: ceramics, cermets, and metals. Each group provides different advantages and limitations as compared with the established carbon anodes [2–6]. In general, new materials must provide a proper electrical conductivity, withstand the highly corrosive vapours and melts of fluoride salts, provide physical and mechanical stability between room temperature and approx. 1.000 °C, resist the thermal shock, provide inertness in molten aluminium, and have economic efficiency. Replacing carbon anodes from the primary aluminium production also facilitates the elimination of polycyclic aromatic hydrocarbons (PAH) and sulphur compound emissions [2]. Recent developments favoured Ni-alloys or SnO_2 inert anode materials [5].

An attempt is the introduction of metal-ceramic composite materials based on widely available components. The intention is the combination of the electrical and mechanical characteristic of the metal phase with the chemical stability of the ceramic phase. In contrast with cermets, the new metal-matrix material promises higher electrical conductivity. CrNi-steels also provide a certain resistance in contact with corrosive salt even at elevated temperature [7,8]. The susceptibility of common steels in contact with molten aluminium is a well-known problem [9–12]. Surface treatments and coatings can provide an improved resistance against molten aluminium attack for future applications as inert anodes in the electrolysis cell [9,13–15].

Beyond the performance of the electrolysis cell, the contamination of the aluminium in case of anode failure or corrosion is a critical aspect. The aim of the present study was the investigation of the corrosion mechanisms of steel-ceramic composite materials immersed in cryolite. The cryolite composition and the thermal conditions were inspired by the industrial smelting flux electrolysis of aluminium. Specimens were prepared from a commercially available 316L steel powder with additions of titania (TiO_2) or magnesia (MgO), respectively. The materials were tested in a salt mixture at 960 °C for 8 h.

2. Material and methods

The matrix material used in the present work was a standard AISI 316L grade steel powder prepared via gas atomisation (TLS, Germany). The chemical composition of the spherically shaped steel powder ($d_{50} = 29 \ \mu m$) is given in Table 1. Composite variants were manufactured from 60 vol% metal and 40 vol% of commercially available MgO or TiO_2 powders. The most important impurities and their concentrations of the irregularly shaped ceramic particles are listed in Table 2. The sintered magnesia type (Refratechnik Steel, Germany) provides particles ranging between 0.2 μm and 350 μm. The fine-grained rutile powder TR-HP2 (Huntsman, Germany) was characterised by a particle size of 0.2–3 μm. The ratios of the d_{50} reinforcement particle size to the matrix'

particle are 1.93 and 0.02 for MgO and TiO_2, respectively. Thus, the titania powder is prone to agglomeration in the interstices between the coarser grained steel particles during mixing and processing. In contrast, rare clustering is expected for 316L/MgO specimens.

The composite variants were prepared via mixing the dry powders in their desired ratio of 0.6 metal and 0.4 ceramic by volume for 90 min using a ball mill with a PET vessel. The compositions were mixed using high-purity yttria-stabilised zirconia balls in order to prevent contamination of the materials. The compact specimens were fabricated by a ceramics-derived extrusion technology [16]. Therefore, an organic binder system was added to the mixed powders to form a plastic paste at room temperature. 1.5 wt% cellulose derivative of type KP3039 (Zschimmer & Schwarz, Germany) and 9.0 wt% (40T) or 11.6 wt% (40 M) of de-ionised water were used for plastification. Additionally, 0.25 wt% of a surfactant (glycerine) and 0.15 wt% of a lubricant (oleic acid) were necessary for sound extrusion. Continuous extrusion provided a strand-shaped geometry using a single-screw extruder of type LK III 2A (Linden, Germany). The shaped test specimens ($150 \times 20 \times 8 \ mm^3$) were cut after extrusion.

The water was removed stepwise from the shaped specimens in an air-circulated dryer, applying a maximum temperature of 110 °C. Then, the specimens were preheated in an oxidising atmosphere in order to ensure sufficient elimination of the organics. The heating and cooling gradients were 1 $Kmin^{-1}$ and the maximum temperature 400 °C. The inert-gas atmosphere sintering of the binder-free specimens was conducted in an electrically heated furnace with a graphite lining (Xerion, Germany). The final consolidation was performed by applying a maximum temperature of 1400 °C for 2 h with heating and cooling gradients of 5 $Kmin^{-1}$. The resulting specimens in their as-fired state were labelled as 40 M (316L/MgO) and 40T (316L/TiO_2), respectively. A second set of specimens was additionally oxidised at 850 °C for 4 h in a gas-heated furnace in order to create the pre-oxidised state (40MO/40TO) with improved corrosion resistance [9,11,13,14].

The samples were tested in their as-fired or pre-oxidised state without any further treatment in a corrosion setup according to Fig. 1. An industry-relevant salt mixture (cf. chemical composition Table 5) was prepared from cryolite (Merck, Germany), AlF_3 (Trimet Aluminium SE, Germany), CaF_2 (Thermo Scientific, Germany), and γ-Al_2O_3 (Merck, Germany). The molar ratio n(NaF)/n(AlF_3) was 2.3. The corrosion equipment was evacuated and flushed with pure argon three times before heating. The anodes were inserted into the molten salt 10 min after reaching the test temperature of 960 °C. All static corrosion tests were stopped after 8 h by moving the sample from the salt into the cooling section with a flushing inert gas atmosphere. Each test was performed with a virgin salt mixture of 800 g. The salt mixtures were mixed and homogenised after tests for chemical and mineralogical analyses. The corroded specimens were cut and polished for microstructural investigations according to Fig. 1. Samples were received from the immersed section ("SC" salt-corrosion) and from the section without any contact to the molten salt ("NSC" no-salt-corrosion). Additionally, the microstructural characterisation of the material variants comprised analyses in the as-fired state and after pre-oxidation without any contact to molten cryolite. All material variants were prepared by conventional grinding and polishing steps followed by vibrational polishing with colloidal silica for 20 h. Chemical analyses of the salt were done with inductively coupled plasma (ICP) after milling.

Microstructural characterisations were conducted using scanning electron microscopy REM-FIB Amber (Tescan, CZ) equipped with Bruker (USA) detectors for energy dispersive X-ray spectroscopy (EDS) of local chemical concentrations. Electron backscatter diffraction (EBSD, Bruker Nano GmbH, Germany) was utilised for the analysis of local crystal structures and orientation relationships. X-Ray diffraction measurements (XRD) were performed with an EMPYREAN (Germany) equipped with a GaliPIX3D detector in Bragg-Brentano geometry.

Analyses with CuKα radiation were conducted in a 2Theta range from 10 to 140° and an effective counting time of 160 s/step for powder

Table 1
Chemical composition of the initial steel powder. Carbon concentration was determined by using combustion analysis, nitrogen concentration by using carrier hot gas extraction and the concentration of other elements by using inductively coupled plasma (ICP) spectroscopy, in wt%.

Cr	Ni	Mn	Mo	Si	C	Ti	Al
16.7 ± 0.0	10.8 ± 0.1	1.61 ± 0.03	2.45 ± 0.02	0.61 ± 0.02	0.027 ± 0.004	0.004 ± 0.000	0.082 ± 0.001

Table 2

Composition of the ceramic components in wt%, n.d. – not detected.

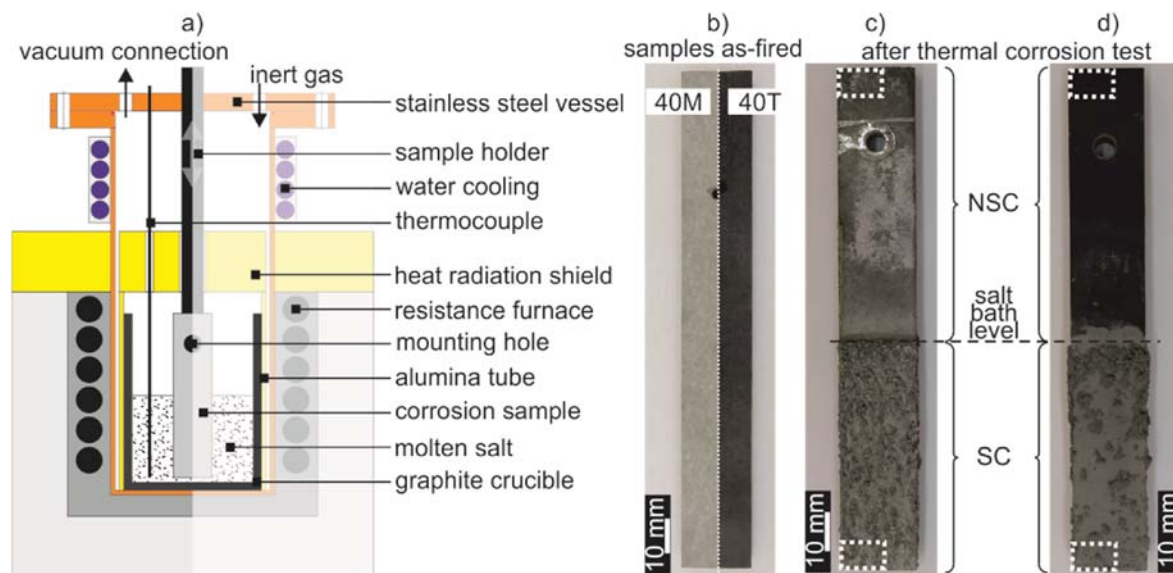| Ceramic	TiO_2	MgO	SiO_2	CaO	Fe_2O_3	Cr_2O_3	Mn_2O_3	Na_2O
MgO	n.d.	97.4	0.47	1.21	0.52	0.01	0.04	0.02
TiO_2	99.7	n.d.	n.d.	n.d.	0.01	n.d.	n.d.	0.001

Fig. 1. Thermal corrosion test: a) schematic experimental setup for the corrosion tests, b) samples before corrosion tests and after corrosion tests in molten cryolite: c) 40 M, d) 40T (white doted boxes indicate sample preparation positions for microstructural analyses in the corrosion section (SC) and in the atmosphere section (NSC)).

samples. Scans parallel to the sample's corrosion front with a distance of 200 μm to each other were done on polished cross-sections in a 2Theta range from 25 to 100° and an irradiated length of approximately 100 μm. To obtain an acceptable signal/noise ratio for these measurements, the effective counting time was increased to 960 s/step. All XRD pattern were obtained using a step size of 0.014°. Qualitative analyses were performed using X'Pert HighScore Plus software (Malvern Panalytical B. V., Netherlands) with the Inorganic Crystal Structure (ICSD) database (FIZ Karlsruhe GmbH, Germany). The investigations on the expansion of the corrosion progress were complemented by measurements using a laser scanning microscope VHX-1000 (Keyence, Germany).

Statistical chemical evaluations were performed using automatic feature analysis. EDS elemental mappings were generated using PSEM express (ASPEX, FEI, USA) with an acceleration voltage of 20 kV. Three individual rectangular sections were scanned for each material. The average nominal concentration of each element was calculated using the EDS images (2048 × 2048 pixels in resolution) for the examination of inhomogeneities in the composite materials. Averaging the grayscale value for each pixel line in the x- and y-direction and relating the obtained values to the global mean grayscale value of the image results in the nominal concentration of the respective element parallel and perpendicular to the direction of extrusion.

The true density (ρ_{tr}) of the as-delivered metal and ceramic powders was determined with a Helium pycnometer AccuPyc 1340 TEC (Micromeritics, USA). Bulk density (ρ_b) and open porosity (OP) of the composite specimens were determined according to the principle of Archimedes as given in standard DIN EN 623 using water as immersion fluid. The relative densities (RD) of the composite materials were estimated using the ratio of ρ_b and ρ_{tr} of the starting powders. The linear shrinkage after sintering (S_l) refers to the dimensional change refers to the dimensional change between the dry state and the as-fired state.

3. Results and discussion

3.1. Characterisation of the as-fired state

The as-fired specimens exhibited a glossy metallic surface due to the high-purity argon atmosphere inhibiting appreciable oxidation during sintering. The 316L/TiO_2 specimens possessed a significantly lower open porosity as compared with the 316L/MgO variants (cf. Table 3). The uncertainty of the actual phase composition in the as-fired or pre-oxidised materials must be taken into account in the assessment of the estimated relative density. The pre-oxidation lead to a weight gain of (5.00 ± 0.43) % and (0.37 ± 0.03) % for the MgO-containing and TiO_2-containing materials, respectively. As expected, the increase in weight due to oxidation is closely related with a reduction of the open porosity for both material variants. Due to the higher porosity, MgO-containing specimens are more likely to be affected by the infiltration of molten salt during corrosion tests as compared with the TiO_2-containing specimens.

Differences in the consolidation during sintering comparing the 40 M and 40T materials are likely to be affected by the characteristics of the as-delivered ceramic powders. In particular, the particles size distributions and the morphology differ between the MgO and the TiO_2 powders. Also the common sintering temperature of MgO and TiO_2 are

Table 3

Physical characteristics of the materials in their as-fired state and after the additional pre-oxidation.

Material	40 M	40MO	40T	40TO
S/%	8.6 ± 1.2	–	9.5 ± 0.7	–
ρ_b/g·cm^{-3}	4.84 ± 0.05	5.00 ± 0.05	6.02 ± 0.02	6.00 ± 0.01
OP/%	21.4 ± 0.9	12.6 ± 0.4	4.8 ± 0.3	1.6 ± 0.1
RD/%	77.8 ± 0.8	80.5 ± 0.7	92.6 ± 0.3	92.3 ± 0.1

widely different [17,18]. However, the thermal processing of the composite materials is limited by the melting of the steel exceeding $\approx$1400 °C. The as-delivered steel powder consisted of (82 $\pm$ 2) % austenite. The remainder was martensite or δ-ferrite that cannot be reliably distinguished using X-ray diffraction due to their body centred cubic crystal structure. X-ray diffraction and EBSD analyses of both as-fired composite materials revealed the preservation of the steel in a mostly austenitic structure. However, deviations in the diffraction patterns indicate changes in the metal structure.

Fig. 2 illustrates the characteristic coarse-grained microstructure and the elemental mapping of the 316L/MgO specimens in their as-fired state. Metal and ceramic sections are clearly recognisable forming an interpenetrating composite. Zhang et al. [19] reported the formation of a metal-matrix composite after sintering 316L/zirconia with a minimum proportion of 60 vol% metal. Nevertheless, the metal and ceramic sections are homogeneously dispersed and no clustering occurred during sintering. Coarsening during heat treatment is not recognisable for the magnesia particles and the irregular shape of the raw material is still present. Consolidation of the 316L is rare, but the morphology of the metal proportion changed forming fissured steel grain boundaries and metal-ceramic interfaces during sintering. Local peak concentrations of the metal or ceramic components are scarcely visible, except for some coarse-grained MgO-particles. Distinct regions of high Mg concentrations without noticeable quantities of the main steel elements and vice-versa clarify the absence of chemical interactions during (thermal) processing. Especially Cr and Mn are prone to inter-diffusion during conventional sintering at temperatures slightly below the melting temperature of the Cr–Mn–Ni steel [20]. Segregations of Ni and Cr forming martensite or ferrite within their original steel particles were also not detected [21,22]. Statistical evaluations of the metal and/or ceramic particles using an automated feature analysis (AFA) failed because of large expansion and merging regions instead of isolated particles dispersed in a continuous matrix material as previously shown [21].

Detailed SEM investigations on the as-fired materials confirmed the obtained results. The microstructure (see Fig. 3a) and characteristic chemical concentrations of the metal and of the ceramic particles determined by EDS as given in Table 4 are in good agreement with the raw materials (cf. Tables 1 and 2). Minor quantities of Cr, Mn, and Fe detected in the oxide particles via EDS cannot reliably be distinguished between the surrounding material and the ceramic particles. The Mg/O-ratios in sections labelled *ceramic* refer to stoichiometric MgO considering the accuracy of oxygen detection using EDS and which was proven by X-Ray diffraction with the identification of periclase (#ICSD 64928).

The microstructure of material 40T largely differed from the complement with magnesia, even having the same volume fractions of steel and ceramic (cf. Fig. 3b and 4). The majority of the metal remained in a spherical shape with some coalescence. In general, coalescence and grain growth are less pronounced as compared with the 40 M material. The steel particles are surrounded by a continuous fine-grained ceramic section. Intentionally, 60 vol% of 316L were expected to form a continuous metal matrix or at least an interpenetrating microstructure with the ceramic counterpart [19,23]. The inhibiting effect of fine-grained titania on the sintering progress of high alloyed CrMnNi steel was already reported for lower ceramic/metal ratios whereas the coalescence of TiO_2 during sintering at 1400 °C is in accordance with expectations [12,24].

In addition, the significantly smaller TiO_2 particles (as compared with MgO) were expected to accumulate in the interstices of the coarser-grained steel [23]. Rather, a continuous non-metallic matrix consisting of titania with some impurities and isolated metal particles formed during sintering. The local concentrations of the most important elements are summarised in Table 5. The susceptibility of Mn and Cr to diffusional interchange and accumulation in certain ceramics is well-known for the sintering of similar composite materials [21,25]. In detail, these phenomena are associated with a loss of approx. 22% Cr and 75% Mn in the steel particles as compared with the as-delivered chemistry (cf. Table 1). It must be considered that the oxygen quantification by EDS is inaccurate and involves large errors preventing reliable stoichiometric calculations.

Here, two distinct ceramic phases were formed during sintering. The one referred to as *ceramic I* with molar Ti/O ratios of $\approx$0.45 and *ceramic II* with Ti/O ratios of $\approx$0.5. These fluctuations indicate the formation of Ti-suboxides during inert-gas sintering.

Delamination or broken-out particles could hardly be detected, which indicates a strong bonding at the metal/ceramic interfaces. Accordingly, the formation of distinct interlayers was not detected by the used methods [26,27]. Nevertheless, the apparent porosity is significantly lower than in the 40 M material and dominantly located within the ceramic phase (see Fig. 3b black regions).

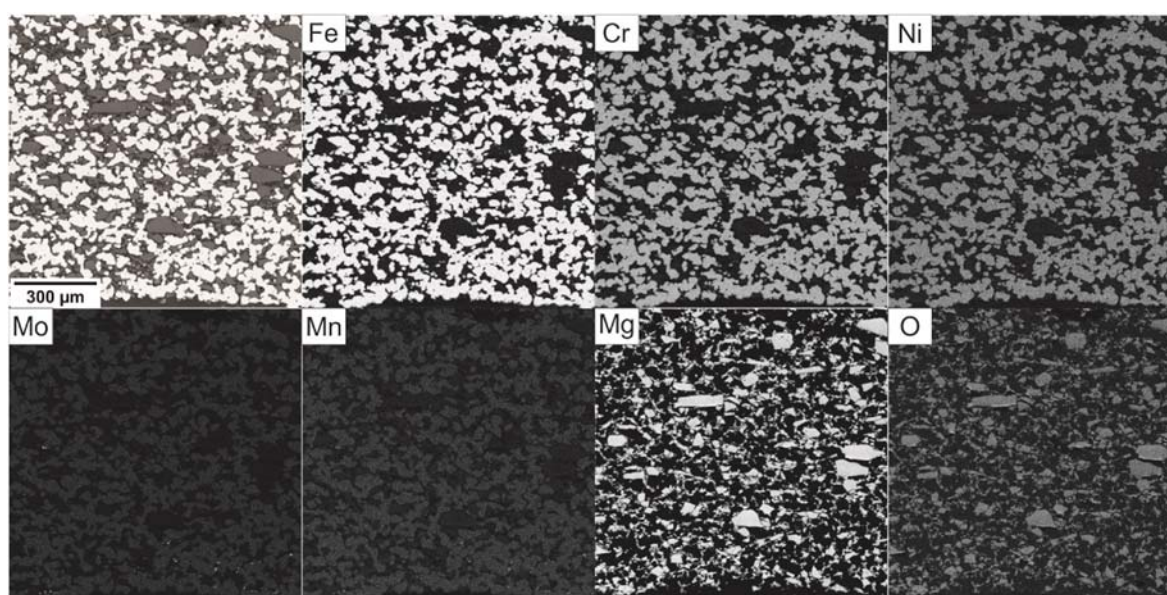The directional concentration of elements of interest was calculated

Fig. 2. SEM image (BSE contrast) showing loosely packed ceramic particles (dark grey) and steel particles (light grey) with porosity (black) and the corresponding EDS mappings of the most relevant elements for the 40 M specimens.
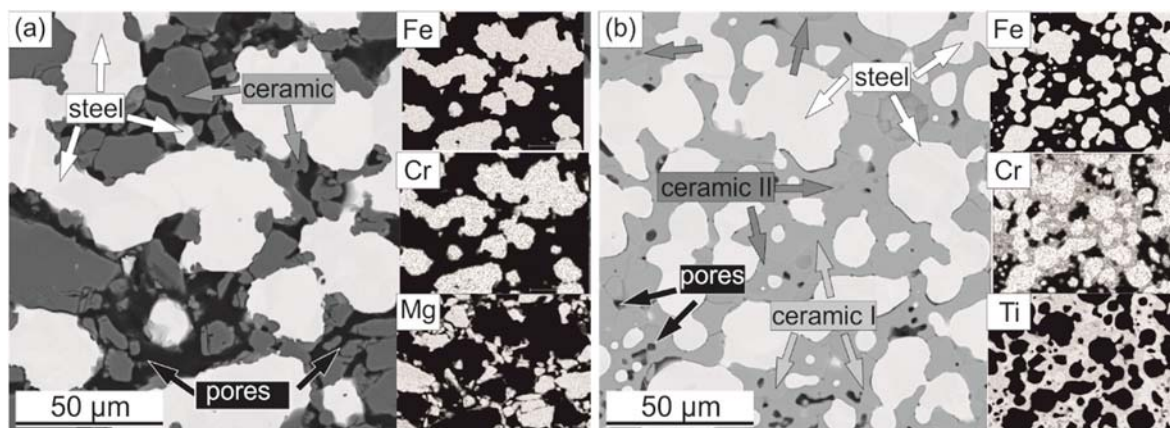
Fig. 3. Microstructure of the materials after firing and polishing illustrating the presence of steel, ceramic particles, and certain porosity: SEM (BSE) images of a) 40 M and b) 40T with EDS mappings of a few elements.

Table 4
Average chemical composition (EDS) of the as-fired 40 M material (cf. Fig. 3a) in wt%, n.d. – not detected.

classification	Fe	Cr	Mn	Ni	Mo	Si	Mg	O
steel	69.1 ± 0.1	17.1 ± 0.1	0.9 ± 0.0	10.6 ± 0.1	2.2 ± 0.0	0.1 ± 0.0	0.1 ± 0.0	n.d.
ceramic	0.7 ± 0.4	1.0 ± 0.2	0.8 ± 0.1	n.d.	n.d.	n.d.	58.4 ± 0.2	39.0 ± 0.3

Table 5
Average chemical composition (EDS) of the 40T material in wt% (cf. Fig. 3), n.d. – not detected.

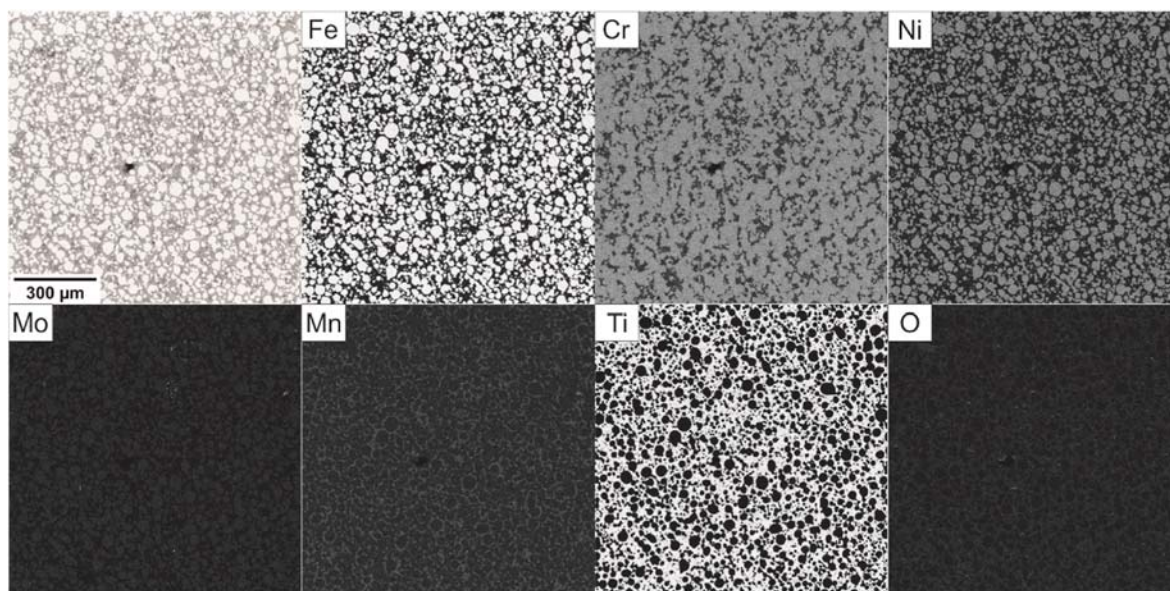| classification	Fe	Cr	Mn	Ni	Si	Mo	Ti	O
steel	71.9 ± 0.1	13.1 ± 0.2	0.4 ± 0.0	11.2 ± 0.1	0.4 ± 0.1	2.6 ± 0.1	0.4 ± 0.1	n.d.
ceramic I	0.6 ± 0.1	13.1 ± 0.0	4.0 ± 0.1	n.d.	n.d.	n.d.	47.5 ± 0.2	34.9 ± 0.2
ceramic II	1.2 ± 1.0	4.3 ± 0.2	1.9 ± 0.1	n.d.	n.d.	n.d.	54.3 ± 1.0	38.3 ± 1.7

Fig. 4. SEM image (BSE contrast) showing largely embedded ceramic (dark grey) and individual steel particles (light grey) with few pores (black) in the cavity and the corresponding EDS mappings of the most relevant elements for the 40T specimens.

in order to investigate the homogeneity of the composite materials and possible manufacturing-related alignments of the ceramic particles. Fig. 5 illustrates the average nominal concentration of elements based on the elemental mappings shown in Figs. 2 and 4, i.e., the average concentration of an element in a pixel line related to the global mean concentration of that element. In this regard, positive values indicate a higher concentration of that element compared to the global mean, while negative values indicate a lower value.

Accordingly, the Mg and Ti concentrations are presented for 40 M and 40T composite materials, respectively. Clearly, no alignment of the
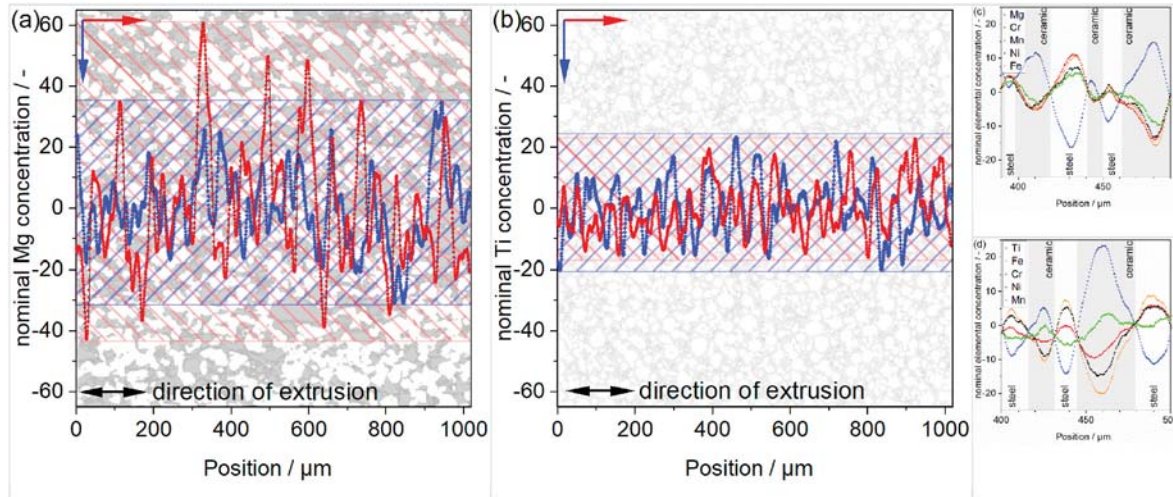
Fig. 5. Orientation and dispersion of the ceramic particles in the metal matrix as detected with the ASPEX-EDS-signals of Mg and Ti in a) 40 M and b) 40T composite materials, respectively (x-direction parallel with the direction of extrusion); distinction of metal- and ceramic-rich sections for the c) 40 M and d) 40T composite materials at higher magnification, indicating the diffusion of Mn into TiO$_2$ within the 40T sample.

fine-grained titania particles can be derived from the Ti concentrations, as the Ti concentrations scatter to the same extent in both directions. In contrast, the scattering in the nominal Mg concentrations within the 40 M composite material was larger in the direction of extrusion compared to that perpendicular to the direction of extrusion. Such differences indicate the alignment of magnesia particles with the direction of extrusion as a result of the extrusion process itself. In comparison, the spherical metal particles are equiaxed in both composite variants. Fig. 5c and d shows an extract of Fig. 5a and b, respectively supplemented by the nominal concentrations of the main elements of the steel (Fe, Cr, Mn, Ni). It can be seen that regions with high nominal Mg concentration showed a lower nominal concentration of the elements expected in the steel matrix for the 40 M sample (Fig. 5c). A similar result was observed for the 40T sample where regions of high nominal Ti concentration showed a lower nominal concentration of Fe and Ni (Fig. 5d). However, Ti-rich regions showed large nominal Mn concentrations as well, i.e., a higher Mn contentration compared to the global mean concentration of Mn. This fact indicates the accumulation of Mn in the initial TiO$_2$ particles. Cr was contained in the ceramic particles of the 40T sample as well (Table 5). However, its average concentration in the ceramic particles was still lower compared to that of the steel matrix and thus the global mean concentration, which is indicated by the negative nominal

concentration of Cr in Ti-rich regions (Fig. 5d).

Analyses of the materials with the additional pre-oxidation process revealed microstructural changes (see Fig. 6). In detail, the oxidation process of composites did not lead to a considerable oxidation of the steel particles, neither at the outside nor at the centre of the material. This observation is consistent with the similar physical properties obtained for the 40T and 40TO8 specimens. However, X-Ray diffraction patterns of the pre-oxidised 316L/TiO$_2$ materials indicated the formation of magnetite Fe$_3$O$_4$ (see Fig. 7) whereas Ti$_3$O$_5$ was identified before and after pre-oxidation. Some peaks could not be reliably assigned to crystal structure according to ICSD and which indicated the formation of Ti-suboxides. In contrast, the weight gaining oxidation of 316L/MgO was closely related with the formation of oxide layers surrounding the steel particles. EDS mappings indicated the blurred distribution of Fe and Cr after the pre-oxidation as compared with the as-fired state. EDS analyses revealed the formation of oxides containing roughly 42 at% Fe, 25 at% Cr, and 15 at% Ni and minor fractions of Mo and Mn. These sections were detected on the surface of the initial steel particles but not forming a seamless coating and identified as spinel-type using EBSD. The formation of FeCrNi(Mn) spinel with mutual phase transitions is well known for the oxidation of stainless steels [26,28,29]. Additionally, a cubic crystal structure was detected using EBSD in the interstices of the
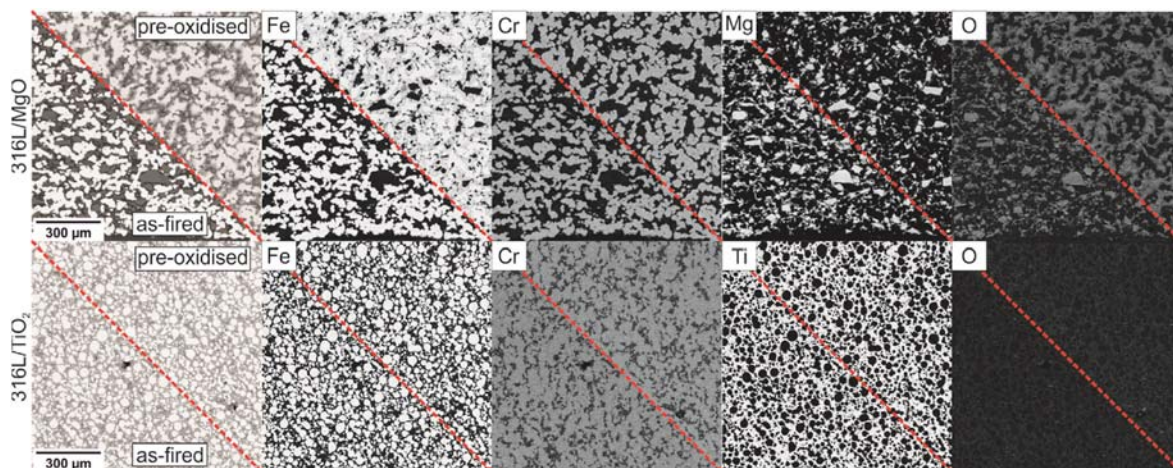

Fig. 6. SEM images (BSE contrast) of both material variants before and after the pre-oxidation process and the corresponding EDS mappings of the most relevant elements for the oxidation.
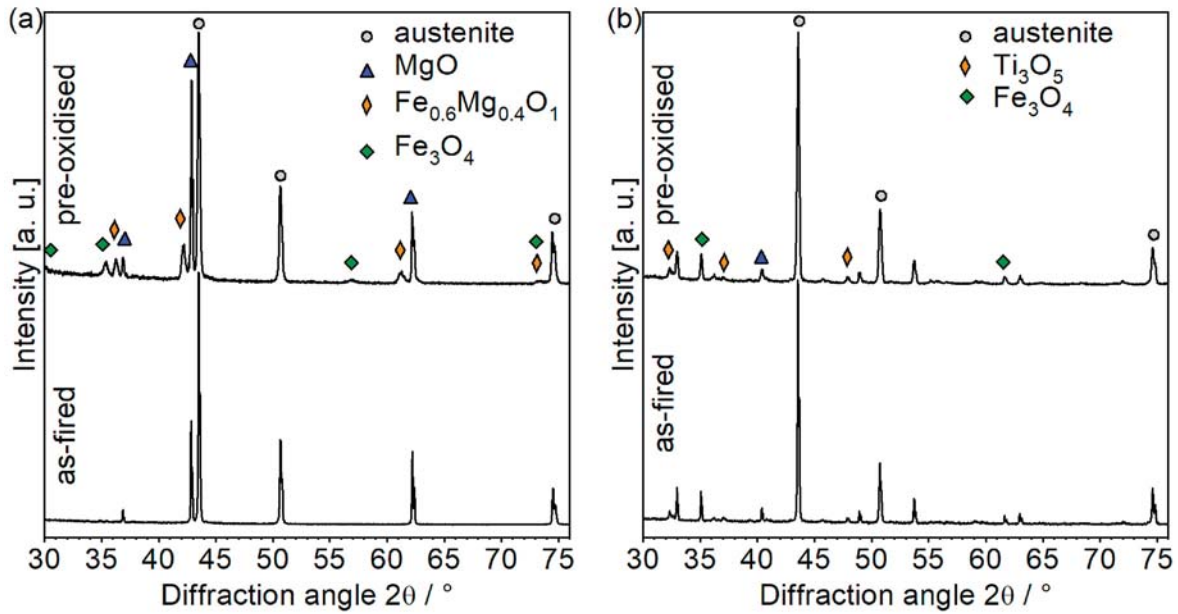
Fig. 7. X-ray diffraction patterns of the material variants in their as-fired state and after pre-oxidation: (a) materials with 316L/MgO – identified ceramic phases: periclase (#ICSD 64928) and matching structures for minor phase $Fe_{0.6}Mg_{0.4}O$ (#ICSD 60696), and magnetite (#ICSD 65338) and (b) material variants 316L/TiO_2 – identified ceramic phases: Ti_3O_5 (#ICSD 50984), and magnetite (#ICSD 96012).
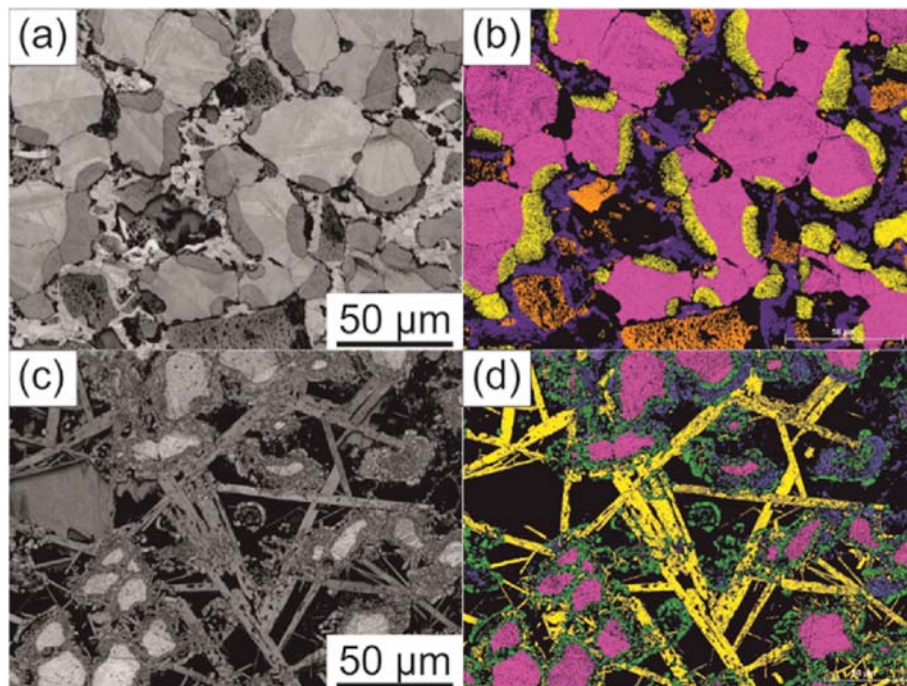

Fig. 8. EBSD mappings of the pre-oxidised material 316L/MgO before (a–b) and after (c–d) the corrosion test with the image quality mappings (a/c) and the corresponding EBSD mapping (b/d), phases identified using EBSD for b): pink/austenite, orange/periclase, yellow/Fe–Cr–Ni-spinel, blue/Mg–Fe–O; and d): pink/austenite, green/steel without Cr, blue/Mg–Fe–O; yellow/corundum.

steel and the magnesia particles and which roughly corresponds to the chemical composition $Fe_{0.5}Mg_{0.3}O_{0.2}$ according to EDS signal. X-Ray diffraction analyses have largely confirmed these results: the ceramic fractions were identified as periclase (#ICSD 64928) or $Fe_{0.6}Mg_{0.4}O$ (#ICSD 60696).

3.2. Analyses after thermal corrosion tests

3.2.1. General aspects

Investigations of the specimens after the corrosion tests with molten salt at 960 °C revealed significant changes throughout all materials tested (cf. Fig. 1 c/d). Powder X-Ray diffraction pattern of the molten salt mixture without any corrosion material provided a reference composition of roughly 35% chiolite ($Na_5Al_3F_{14}$), 53% cryolite, 10% verneite ($Na_2Ca_3Al_2F_{14}$) and the remainder corundum (Al_2O_3). Analyses

of the salt mixtures after the corrosion tests clarified not only reactions within the salt mixture but also with the test specimens (see Table 6). Minor concentrations of Fe, Cr, and Mn indicate some dissolution of the steel within the molten salt irrespective of the ceramic component. However, elevated concentrations of Mg or Ti in the salt mixture are attributed to corrosion-driven dissolution of the ceramic components from the test specimens 40 M/40MO and 40T/40TO, respectively. Considering the initial composition of the test specimens and the salt/sample ratio revealed a dissolution of 22–24% MgO from the composite materials in the salt by weight. The solubility of MgO in cryolite melts is lower compared with the solubility of alumina [30,31]. But the reaction of MgO and AlF$_3$ forming MgF$_2$ and Al$_2$O$_3$ was expected to enhance the dissolution of the MgO particles [30,31]. The loss of the ceramic component after corrosion amounts only half the quantity in case of TiO$_2$-containing composite materials.

A general aspect is the infiltration of both composite materials with the molten salt. EDS elemental mappings proved the saturation of the complete test specimens 40 M even above the bath level based on the presence of Na and F (Fig. 9). Yet, no corrosion was detected in these sections for the as-fired and the pre-oxidised specimens. Similar results were obtained for the 40T test material.

3.2.2. 316L-MgO-system

EDS elemental mappings and complementary SEM/EDS/EBSD-analyses identified a corrosion layer in material 40 M (Fig. 10) covering a uniform expansion of (1160 ± 87) μm in the bath zone. Here, the material suffered from the leaching of the MgO particles during corrosion resulting in marginal Mg-concentrations. The locations of initial magnesia particles were replaced by infiltrated molten salt with fluctuating concentrations of 40–63 mol% F, 16–49 mol% Na, 10–14 mol% Al, and ≤12 mol% Ca at CR-ratios of 1.5–4.7. EBSD-analyses revealed the presence of cryolite with certain crystallographic distortions. The quantity of (0.3 ± 0.2) wt% Mg corresponds to the results of ICP-measurements of the molten salt. In contrast, the steel composition in the leached layer is uniform in Fe, Cr, Ni, Mn, and Mo concentrations with the as-fired state and which remains austenitic according to EBSD. Exceeding the clearly delineated leached layer (section I) revealed a second layer with columnar precipitations enriched of aluminium and oxygen with a molar Al/O-ratio of 0.7 (section II). These structures were clearly identified as corundum using EBSD which agrees with the depletion of Al in the salt mixture (cf. Table 6). The precipitation layer exhibits a spread of 300–400 μm with a blurred distinction from the core material (section III). This inner section represents the majority of the specimen after the corrosion test with the non-metallic components periclase, cryolite, and MgF$_2$ according to EBSD. The latter is non-critical and a widely used additive in melt refinement to improve e.g. the current-efficiency of the electrolysis cell [32,33]. Adding MgO with the subsequent reaction with AlF$_3$ from the salt mixture giving MgF$_2$ and Al$_2$O$_3$ is a cost-efficient alternative and common chemical process.

While the steel particles were identified as austenite, severe ancillary reactions were observed. The outer shell of steel particles possessed lower Cr concentration as compared with the centre of the particles. The reliable identification of the skin and additional structures with high concentrations of Mg–Al–Cr–O were hampered by the small extension of a few microns. Kikuchi patterns suggest cubic crystal structures for these sections with some uncertainty.

Fig. 11 shows gradual X-ray diffraction patterns of the corrosion front which proved the dissolution of the ceramic particles from the composite material in the molten salt mixture. Alumina was detected only in a range of the four consecutive measurements i3-i9 (expansion ≈800 μm) and identified as the hexagonal corundum (#ICSD 30024). MgO peaks were marginally detected in the intermediate scan (i7) in the centre of the corrosion layer. These peaks fully disappeared upon exceeding the precipitation layer (i9) and in the leached corrosion layer scans i11 and i13 (cf. Fig. 10). Neighborite (NaMgF$_3$) was determined using X-Ray only at the corrosion front (i3) what suggests an intermediate composition in the corrosion process.

The pre-oxidation prior to corrosion tests resulted in a reduction of the leached layer (section I) to (277 ± 24) μm in the bath zone. The resulting structures provide similar columnar precipitations (cf. Fig. 8) as compared with the as-fired material after corrosion tests according to their morphology. But the chemical composition differs giving an average of 48 at% Al, 20% at% Cr, and 31 at% oxygen using EDS.

3.2.3. 316L-TiO$_2$-system

Fig. 12 illustrates the microstructure of material 40T after thermal corrosion test. The corrosion layer of (463 ± 20) μm in the corrosion zone is less than half the expansion measured for specimens containing MgO. The steel was detected as austenitic (EBSD) in both, the corrosion layer and the core material. The chemical composition largely agreed with the as-fired state with deviations of ≤1.0 wt% (Fe, Cr) or ≤0.2 wt% (other elements). The initial TiO$_2$-particles almost completely disappeared in the corrosion layer and were replaced by the infiltrated molten salt with concentrations ranging from 45 to 56 mol% F, 20–39 mol% Na, 10–20 mol% Al, and ≤1 mol% Ca (CR-ratios 1.1–3.9) according to EDS. The concentration of the main steel elements Fe, Cr, Ni, Mo, and Mn was 1 wt%. Ti concentrations of 0.09–0.11 wt% were detected, which is less than half the concentrations measured for the surrounding salt mixture with ICP. The material was identified as cryolite with some crystal distortions by EBSD-analyses. Other phases were not observed in the corrosion layer using SEM/EBSD. Specimens with titania possessed a distinct corrosion front without an intermediate section as observed for the 40 M specimens. The remaining ceramic particles consisted of 28–33 mol% Ti and 62–64 mol% O. Molar Ti/O-ratios of 0.44–0.54 indicate the presence of both, oxygen-lean and oxygen-rich TiO$_x$. The identification of the crystal structure was hampered by super-positioned monoclinic EBSP indicating Ti$_3$O$_5$ or CrTi$_2$O$_5$. Also, a clear distinction between these phases in the composite material using X-ray diffraction (cf. Fig. 13) was not successful. However, the chemical concentrations emerged from EDS cannot clearly exclude one of both. The solid solubility of Ti$_3$O$_5$ and CrTi$_2$O$_5$ at the present molar Cr/Ti-ratios of 0.10–0.25 and known complex thermally induced transformations give strong evidence for the coexistence of both phases [34,35]. Both compounds are prospective anode materials for solid oxide fuel cells according to their electrical conductivity and may also provide the desired properties for future inert anode materials.

4. Conclusions

Metal-ceramic composite materials were fabricated with the ceramics-derived extrusion process at ambient temperature. The thermal consolidation via pressureless sintering at 1400 °C provided two materials with different micro- and macrostructures. The combination of steel powder and fine-grained titania resulted in the formation of a ceramic matrix with embedded steel particles with less than 5% open
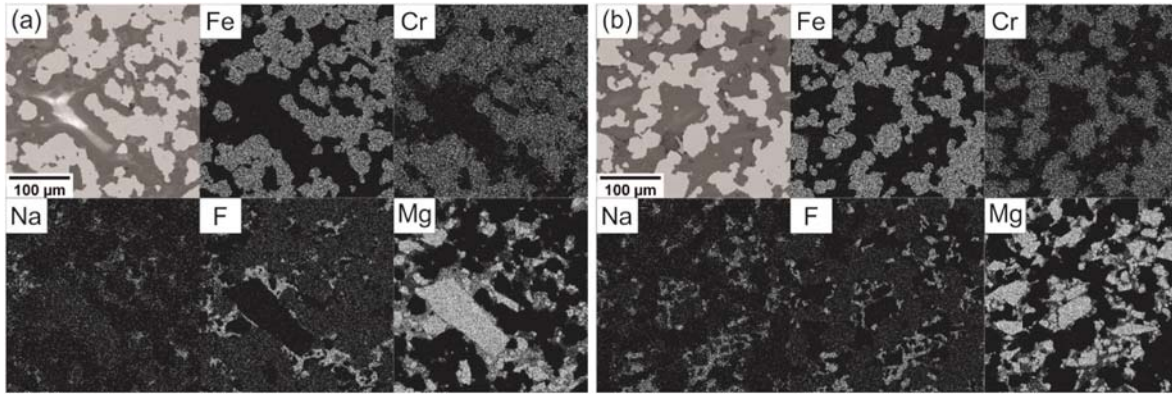
Table 6
Chemical compositions of the salt mixture before and after corrosion tests determined by ICP in wt% and the molar cryolite ratio (n.m. not measured).

Sample condition	Pure cryolite mixture		With corrosion test material			
	Powder	Molten without test material	40T	40TO	40 M	40MO
Na	25.1	24.6	24.9	25.1	24.0	24.6
Al	13.8	15.9	15.0	15.2	14.1	14.7
F	50.0	49.7	n.m.			
Ca	2.96	2.92	2.86	2.99	2.78	2.88
Mg	0.00	0.00	0.03	0.03	0.37	0.33
Ti	0.00	0.00	0.26	0.25	0.00	0.00
Fe	0.00	0.01	0.02	0.07	0.02	0.03
Cr	0.00	0.00	0.07	0.07	0.01	0.04
Mn	0.00	0.00	0.02	0.02	0.01	0.01
NaF/AlF$_3$	*2.13*	*1.82*	*1.95*	*1.94*	*2.00*	*1.97*

Fig. 9. SEM images (BSE contrast) of the centre of the samples in the a) SC section and the b) NSC section and the corresponding EDS mappings of some elements indicating the salt infiltration for the as-fired 40 M material.
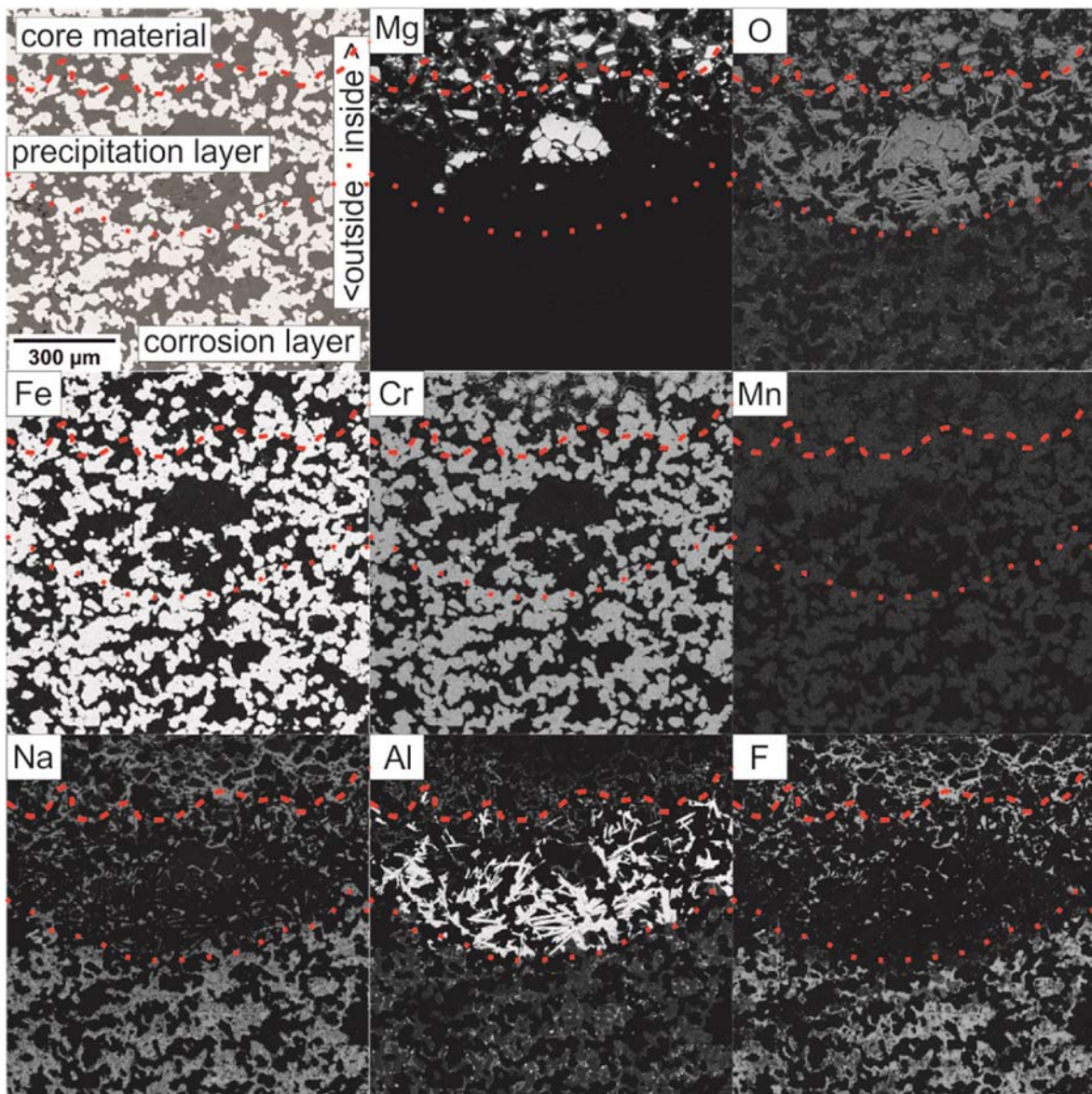

Fig. 10. SEM image (BSE contrast) of material 40 M after corrosion test and the corresponding EDS mappings of most relevant elements for the composite material and the salt bath (the corrosion section with precipitation of corundum is enclosed from the corrosion layer (dotted lines) and the remaining core material (dashed lines).
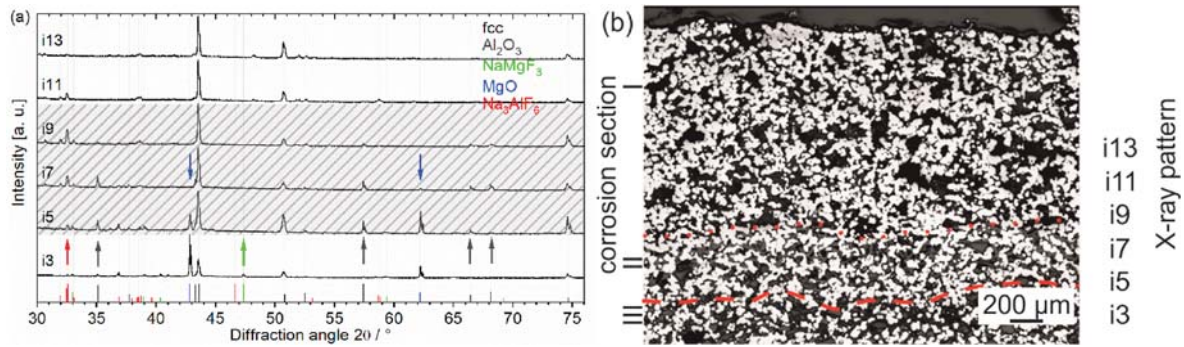
Fig. 11. Corrosion in the 40 M material: a) X-ray diffraction patterns parallel to the sample's corrosion front and b) schematically drawing of the measurement positions (corrosion section cf. Fig. 10).
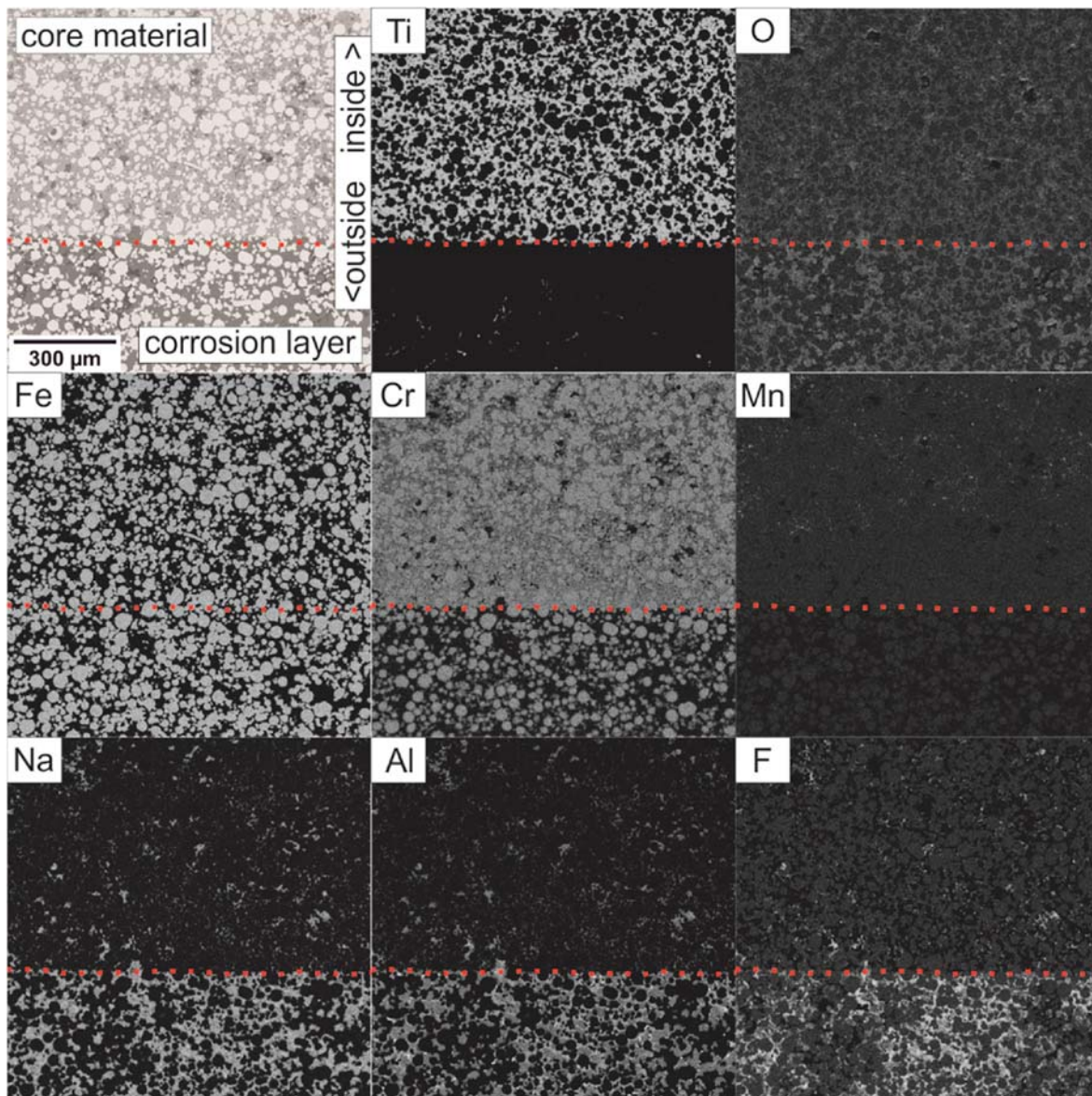

Fig. 12. ASPEX/SEM-micrograph (a) of material 40T after corrosion test the and the corresponding EDS mappings (dotted line indicates the corrosion front).

porosity. Diffusional interactions between the metal and the ceramic component caused a heterogeneous ceramic material. Two different phases were identified with differences in their Ti/O-ratio and the concentrations of Fe, Cr, and Mn. In contrast, the combination of magnesia particles with 316L steel is marked by the absence of significant diffusion and chemical interactions. The microstructure consisted of randomly embedded MgO particles in a porous metal matrix. The pre-oxidation of the material variants resulted in the formation of a
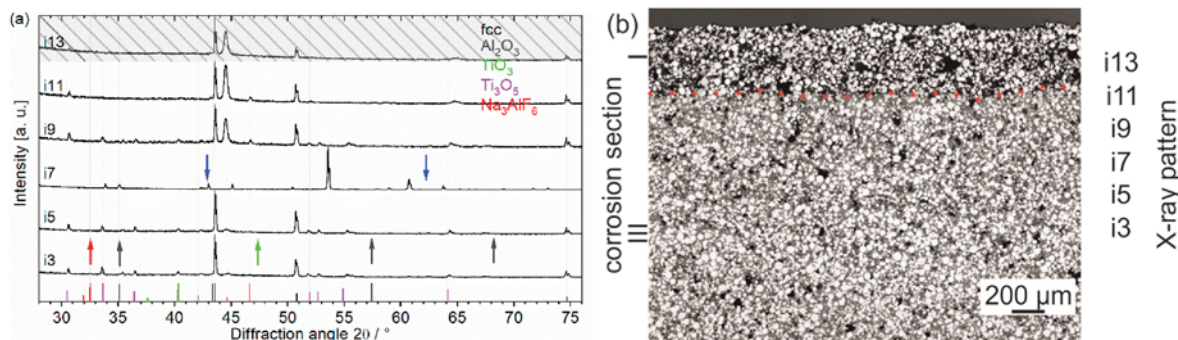
Fig. 13. Corrosion in the 40T material: a) X-ray diffraction patterns parallel to the sample's corrosion front and b) schematically drawing of the measurement positions (section indicates cf. Fig. 12).

Fe–Cr–Ni spinel-type structure and a cubic Fe–MgO-structure. The 40T material was marginally affected by the oxidation process.

In summary, the results of thermal corrosion tests in a synthetic cryolite melt at 960 °C for 8 h demonstrate different corrosion phenomena in 316L-ceramic composite materials with TiO_2 or MgO particles. More specifically, the microstructural characterisation led to the following conclusions:

- Both materials were completely infiltrated by the cryolite even in the non-immersed area.
- The corrosion progress is driven by the dissolution of the ceramic particles (MgO) or ceramic matrix (TiO_2) in the cryolite melt. Differences in particle size of the ceramic and the as-fired density marginally affected the corrosion. The formation of neighborite seems to be the intermediate step in the MgO-corrosion with the simultaneous precipitation of columnar corundum. Similar phases were not identified for the corrosion of 316L/TiO_2.
- The remaining metal structure is widely corrosion resistant and shows no dimensional changes or wear. The chemistry of the corroded steels equals the as-fired state with negligible deviations according to the EDS measuring accuracy.
- The pre-oxidation of the composite materials at 850 °C crucially hampered the destruction during corrosion tests in molten cryolite for both material variants. The expansion of the corroded outer layer was reduced by 15% (316L/TiO_2) or 75% (316/MgO) for the pre-oxidised materials as compared with the as-fired state.

Thermal corrosion was tested but corrosion mechanisms under applied current (electrolysis conditions) are tremendously different. Oxygen formation at the anode may lead to protective environment for the ceramic outer layer and will be further investigated.

The electrical conductivity of the anode material is fundamental in the Hall-Héroult-process. Future measurements of the conductivity and resistivity, respectively, will contribute to understanding the effects of microstructural changes during processing (firing and pre-oxidation) of the metal-ceramic-composites. Issues concerning the semi conductive characteristics of oxygen-lean TiO_x (namely Ti_3O_5) may cause additional effects. Alternatively, portions of electrical highly conductive $CrTi_2O_5$ can contribute to improved properties of prospective anode material based on steel. In addition, the effects of the phases formed in pre-oxidised composites with MgO (i.e. MgF_2 and Al_2O_3) immersed in molten salt are of further interest.

Declaration of competing interest

The authors declare that they have no known competing financial interests or personal relationships that could have appeared to influence the work reported in this paper.

References

[1] F. Habashi, in: G.E. Totten, D.S. MacKenzie (Eds.), Handbook of Aluminum, vol. 2, 2003. New York Basel.
[2] H. Kvande, W. Haupin, JOM 53 (2001) 29.
[3] M.M. Gasik, M.I. Gasik, in: G.E. Totten, D.S. MacKenzie (Eds.), Handbook of Aluminum, vol. 2, 2003, p. 47. Yew York, Basel.
[4] D.R. Sadoway, J. Miner. Met. Mater. Soc. 53 (2001) 34.
[5] R.P. Pawlek, in: W.A. Schneider (Ed.), Light Metals, 2002, p. 1126.
[6] A. Sohlheim, in: O. Martin (Ed.), Light Metals 2018, Springer, Cham, 2018, p. 1253.
[7] G. Zheng, K. Sridharan, JOM 70 (2018) 1535.
[8] Y. Wang, S. Zhang, X. Ji, P. Wang, W. Li, Int. J. Electrochem. Sci. 13 (2018).
[9] D. Wang, Z. Shi, Appl. Surf. Sci. 227 (2004) 25.
[10] P. Malczyk, M. Mandel, T. Zienert, C. Weigelt, L. Krüger, J. Hubálková, G. Schmidt, C.G. Aneziris, Materials 15 (2022) 6723.
[11] P. Malczyk, T. Zienert, F. Kerber, C. Weigelt, S.O. Sauke, H. Semrau, C.G. Aneziris, Materials 13 (2020) 4737.
[12] C. Weigelt, N. Brachhold, R. Eckner, L. Krüger, M. Jhauser, S.O. Sauke, H. Semrau, C.G. Aneziris, Adv. Eng. Mater. 22 (2020), 1901321.
[13] G. Chen, L. Xue, J. Wang, Z. Tang, X. Li, H. Dong, Corrosion Sci. 174 (2020), 108836.
[14] G. Xu, K. Wang, X. Dong, L. Yang, M. Ebrahimi, H. Jiang, Q. Wang, W. Ding, J. Mater. Sci. Technol. 71 (2021) 12.
[15] S. Guo, J. Zhang, W. Wu, Z. Zhou, Prog. Mater. Sci. 97 (2018) 448.
[16] C. Weigelt, C.G. Aneziris, A. Yanina, S. Guk, Steel Res. Int. (2011).
[17] H. Salmang, H. Scholze, Keramik 7 (2007).
[18] I.D. Kasheev, K.G. Zemlyanoi, E.A. Voskretsova, Refract. Ind. Ceram. 59 (2018) 92.
[19] W. Zhang, J. Xie, C. Wang, Mater. Sci. Eng. 382 (2004) 387.
[20] H. Berek, C.G. Aneziris, M. Hasterok, H. Biermann, S. Wolf, L. Krüger, Adv. Eng. Mater. 13 (2011) 1037.
[21] C. Weigelt, F. Kerber, C. Baumgart, L. Krüger, C.G. Aneziris, Adv. Eng. Mater. 23 (2020), 2001215.
[22] C. Weigelt, G. Schmitt, C.G. Aneziris, R. Eckner, D. Ehinger, L. Krüger, C. Ullrich, D. Rafaja, J. Alloys Compd. 695 (2017) 9.
[23] T. Chen, L. Bai, K. Wen, IOP Conf. Ser. Mater. Sci. Eng. (2020) 631.
[24] Yan, Mater. Sci. Eng. 61 (1983) 59.
[25] Dourandish, Mater. Lett. 65 (2011) 523.
[26] W. Mao, Y. Ma, W.G. Sloof, Oxid. Metals 90 (2018) 237.
[27] V.A. Lashgari, G. Zimbitas, C. Kwakernaak, W.G. Sloof, Oxid. Metals 82 (2014) 249.
[28] W. Mao, R.W.A. Hendrikx, W.G. Sloof, Oxid. Metals 89 (2018) 531.
[29] T. Jonsson, H. Larsson, S. Karlsson, H. Hooshyar, M. Sattari, J. KLiske, J.-E. Svensson, L.-G. Johansson, Oxid. Metals 87 (2017) 333.
[30] M. Korenko, F. Šimko, J. Mlynariková, C. Larson, E. Mikšíková, J. Priščák, M. Ambrová, R. Palumbo, J. Mol. Liq. 275 (2019) 535.
[31] N. Leonard, M. Korenko, C. Larson, K. Blood, L.J. Venstrom, S. Nudehi, S. Duncan, R. Diver, F. Simko, J. Príščák, J. Schoer, P.T. Kissinger, R. Palumbo, Chem. Eng. Sci. 148 (2016).
[32] P. Fellner, K. Grjotheim, H. Kvande, Acta Chemica Scandinavia A 38 (1984) 699.
[33] P. Cui, B. Qin, G. M. Khaarberg, J. Electrochem. Soc., 166, D559..
[34] G.P. Shveikin, D.G. Kellerman, V.S. Gorshkov, V.A. Perelyaev, Z. Anorg. Allg. Chem. 544 (1987) 21.
[35] H.J. Steiner, X.M. Turrillas, B.C.H. Steele, J. Mater. Chem. 2 (1992) 1249.